Impact of the blockage ratio on the transport of sediment in the presence of a hydrokinetic turbine: Numerical modeling of the interaction sediment and turbine

Fatima Khaled, Sylvain Guillou, Yann Méar, Ferhat Hadri

Version of Record: https://www.sciencedirect.com/science/article/pii/S1001627921000056
Manuscript_463d25783fe82e5560215d60d4c5b6a2

Impact of the blockage ratio on the transport of sediment in the presence of a hydrokinetic turbine: Numerical modeling of the interaction sediment and turbine.

Fatima Khaled [a,c,*], Sylvain Guillou [a], Yann Méar [a,b], Ferhat Hadri [c]

[a] *University of Caen Normandy, LUSAC, EA 4253, 60 rue Max Pol Fouchet, CS 20082, 50130 Cherbourg-en-Cotentin, France.*
[b] *Conservatoire National des Arts et Métiers, University of Caen Normandy, INTECHMER/LUSAC, Bd de Collignon, 50110 Tourlaville, France.*
[c] *LISV, University of Versailles, 78140 Vélizy, France.*

[*] *Corresponding author*
Email addresses: fatima.khaled@unicaen.fr (Fatima Khaled), sylvain.guillou@unicaen.fr (Sylvain Guillou), yann.mear@lecnam.net (Yann Méar), ferhat.hadri@uvsq.fr (Ferhat Hadri).

Abstract

Interactions between hydrokinetic turbines and near scale and far scale bed sediment particles are considered a critical area of assessment, however, a limited number of research studies have been published to address this issue. The current paper explores the influence of the blockage ratio on the morphology evolution downstream from an hydrokinetic turbine. A modeling framework is derived to predict the significant transport induced by a turbine installed on the erodible fluvial sandy bed surface, such as the Eulerian multi-phase model for the sediment and the Blade Element Momentum Theory (BEMT) for the turbine, using the open source platform OpenFOAM. Two configurations of different blockage ratios are considered. The configurations show differences in the bed morphology and the sediment transport. It has been shown for both configurations that the scour capabilities are enhanced below the turbine due to the acceleration of the flow and increasing local shear stress on the sediment.

Keywords: Environmental impact, Blockage effects, Euler-Euler multiphase, Hydrokinetic turbine, Numerical simulations, OpenFOAM.

1. Introduction

The need for sustainable, predictable energy has led in recent years to the development of projects and studies concerning the installation of Hydrokinetic Turbines (HT) in such high current regions as Alderney Race, Race of Barfleur, The Rhone, among others. Accelerating the use of marine hydrokinetic renewable energy development towards endurance requires investigating interactions between the manufactured environment and its surrounding physical environment. Turbine-sediment interactions are the forefront issue. Exploring turbine-sediment interactions requires intensive research studies in the form of either experiments or numerical simulations or even in situ configurations, which are in progress because there is no effective exploitation yet of the recent projects of installation of hydrokinetic turbines in France. The presence of the turbine could accelerate the flow and lead to local scour (Xia et al., 2010; Shields et al., 2011). It is crucial to ensure the structural safety of the turbine to avoid interruption of energy transmission. In addition, the sediment transport due to the presence of the turbine, could have negative environmental impacts (Shields et al., 2011). This may lead to a change in the site's topography which could result in negative consequences for the environment.

Many numerical investigations have been done in recent years concerning the impact of the presence of hydrokinetic turbines on a regional scale, wherein the turbines' array is represented by a bed friction or momentum sink using the Actuator Disk (AD) theory (Nguyen et al., 2016). The sediment transport is modeled using a classical approach, such as Thiébot et al. (2015) who have modeled the effect of an array of turbines on the sediment transport by placing a 290 MW tidal turbine array in the Alderney Race using a regional two dimensional (2D) hydrodynamic model. They found that the tidal energy extraction has a significant effect on the rate and the pattern of the bed load sediment transport rate on the regional scale. Also Fairley et al. (2015) studied the cumulative impact of HT on sediment transport in the Pentland Firth by applying a three-dimensional coupled hydrodynamic and

sediment transport numerical model. They concluded that the array implementation only has minimal effect on the baseline morphodynamics of large sand banks. Neill et al. (2009) used large grid-cell simulations to assess the impact of an HT array on the sand banks off the northern coast of France. Their study investigated a tidal channel many kilometers long, therefore, their solution lacked the ability to simulate the near-field effects. Gillibrand et al. (2016) have simulated arrays of 1, 4, and 57 tidal turbines, each of 1.5 MW capacity using a three dimensional (3D) hydrodynamic model (RiCOM). The main effect is observed for the array of 57 turbines as an increase in the near-bed velocities and the bed shear stress leading to significant transport of sand.

To date, few studies have evaluated how HT devices modify erodible channels in the vicinity of the device, despite the fact that it is important to develop a holistic understanding as to how these devices affect all aspects of the physical environment at the local scale. Hill et al. (2015) have experimentally shown that the presence of the turbine and the rotation of the blades affect the bed morphology. Musa et al. (2019) have experimentally investigated the local effect of streamwise aligned turbines on the bedload and they found that the geomorphic effects are stronger with increasing shear stress due to the presence of the rotors, inducing an alternating scour-deposition phenomenon. Chen et al. (2017) have investigated the influence of rotor blade tip clearance control on the scour rate of pile-supported, horizontal axis tidal current turbines (TCT) and also attempted to correlate time-dependent scour depth of the TCT with the tip clearance. Their results suggest that the decrease in tip clearance increases the scour depth. In addition, the shortest tip clearance results in the fastest and most substantial sediment transport. Ahmed et al. (2017) studied the fluctuating loads on tidal turbines which are important for fatigue analysis. Computational Fluid Dynamics (CFD) simulations have been done for a geometry-resolved, full-scale tidal-stream turbine and compared with experimental data from a 1 MW machine deployed

at the EMEC test site in the Orkneys. They applied realistic inflow profiles of mean and turbulent velocity fields based on measurements from the deployment site. The simulated velocity field indicates that the turbine rotor influences the axial velocity and the flow turbulence structures to about one diameter 1d upstream of the rotor, while the velocity deficit and enhanced turbulence are extending beyond the 10d downstream.

Very few studies have investigated the local impact of turbines on sediment transport by numerical simulation. In this case, the turbine is finely represented by either the Blade Element Momentum Theory (BEMT) (Malki et al., 2012), the Actuator Line (AL) approach (Apsley et al., 2018) for blades, or even a fully resolved configuration (Grondeau et al., 2017). Yang et al. (2017) have simulated the interaction between an hydrokinetic turbine and bedload sediment transport using large eddy simulation (LES) for the flow, and the Saint-Venant-Exner model (Paola & Voller, 2005) for sediment transport and Actuator Line theory for the turbine blades. Deeper scour and deposition regions are observed when imposing a higher tip speed ratio on the rotors. Chen and Lam (2014) highlighted that the clearance between the rotors and the seabed becomes critical in the turbine induced scour prediction. These results further evidence that the height of tip clearance plays a critical role in designing scour-related units of the turbine. The velocity pattern near the seabed of the turbine has been studied through three-dimensional numerical simulations (Chen & Lam, 2014). They studied the flow pattern between the turbine and seabed. They formulated the hypothesis that the axial component is the largest contributor to the magnitude of velocity. The tangential component was so insignificant that they suggested that the tangential component of velocity has no impact on the scour and deposition process.

Musa et al. (2018) derived and validated a modeling framework to predict the scour induced by Marine Hydrokinetic Turbines installed on fluvial or tidal erodible bed surfaces. The model addresses the problem of bridge pier scour using the phenomenological theory of turbulence. The turbine rotor should be close enough to the sediment that the erosion is

directly caused by the tip vortex shed by the turbine blades, or the rotor should be far enough from the bottom, that the dominant flow features resemble those responsible for bridge pier scour.

Ramirez-Mendoza (2018) have used a series of laboratory experiments and studied the impact of the presence of a horizontal-axis turbine on the flow and a mobile sediment bed. Their results showed a decrease of velocity profiles of about 50% throughout the water column and the flow does not recover after a distance of 15 rotor diameters in the wake. These results may be important to have an idea about effects on the efficiency of turbine arrays on turbine foundations and modifications of coastal sediment transport.

The interaction between HT and the bed morphology in the near wake zone deserves more study at the local scale. In addition, the difficulties and inaccuracies associated with the classical sediment transport modeling approach require the development of other approaches for transport modeling, which are more complete and integrate the complexity of the coupling phenomena between the different modes of sediment transport and hydrodynamics, especially at the grain scale (Guillou et al., 2011). The two-phase Euler-Euler sediment transport model (Barbry et al., 2000; Chauchat & Guillou, 2008; Nguyen et al., 2009) takes into account the majority of physical processes of sediment transport in a two-way interaction, such as the interactions between particles and fluid (Chauchat & Guillou, 2008; Nguyen et al., 2009), the effect of the turbulence of the fluid on the particles, and also particle-particle interactions that are dominant near the sediment bed. The different two-phase models for sediment transport presented in the literature can be differentiated by the choices made by their authors concerning closure models for turbulence or granular constraints (Uh-Zapata et al., 2018). One of the closure models for turbulent stresses is the Reynolds-Averaged Navier-Stokes (RANS) approach. First, a mixing length closure for the diphasic model has been proposed by (Jenkins & Hanes, 1998). This approach has been widely used since then but it is mainly limited to sheet-flow.

More recently, two-equation closure models have been widely used in the literature, including the k-ε model (Bakhtyar et al., 2009; Hsu et al., 2004) and the k-ω model (Amoudry, 2014). Actually, Nguyen et al. (2009) worked on 3D two-phase modeling for sediment transport in geophysical flows.

Until now, no investigation has been done concerning the effect of blockage on the sediment transport in the presence of a hydrokinetic turbine at the local scale. The blockage effects, described by Garrett and Cummins (2007) and Nishino and Willden (2012), were studied especially with respect to the hydrodynamic performance of turbines, such as the study of Consul et al. (2012). They explored the influence of blockage on the hydrodynamic performance of a generic marine cross-flow turbine. They found that increasing the blockage led to an increase in the power coefficient of the turbine. Schluntz and Willden (2015) studied the effect of blockage on rotor optimization using the BEMT. Increased blockage leads to an increased optimal solidity and decreased optimal pitch in terms of blade design.

The current study investigates the blockage effects on the evolution of the sandy bed close to the turbine using a CFD modeling framework. Two configurations A and B are considered with blockage ratios of 0.0168 and 0.0416, respectively, where the blockage ratio is defined as the ratio of the frontal area of the turbine to the area of the flow passage. The methodology, provided in Section 2, is based on the two-phase flow Euler-Euler 3D CFD model used to simulate the sediment transport and the morphology evolution around the turbine (Chauchat & Guillou, 2008; Cheng et al., 2017; Nguyen et al., 2009) and the hybrid analytical 3D Blade Element Momentum Theory (BEMT) used to compute the effect of energy extracted from the turbine on the fluid in the near wake zone (Malki et al., 2012; Shives & Crawford, 2016). The CFD open source library OpenFoam has been used, and the SedFoam code (Chauchat et al., 2017), which is based on the two Phase Euler

Foam code, is applied while introducing the momentum source code of the turbine. The method is validated using the experiments of Mycek et al. (2014) and Hill et al. (2015). Section 3 presents the flume and the turbine blockage effects on the morphology of a bed of sand, exhibiting two configurations A and B with different blockage ratios. The results are then presented over time and at different sections with and without the turbine for each configuration.

2. Numerical methods

2.1. Sediment transport

The mathematical formulation of the Eulerian two-phase flow model is obtained by averaging the local and instantaneous mass and momentum conservation equations for fluid and dispersed particles. The mass conservation equations for the particle phase and fluid phase are written as:

$$\frac{\delta \emptyset}{\delta t} + \frac{\delta \emptyset u_i^s}{\delta x_i} = 0 \quad (1)$$

$$\frac{\delta (1-\emptyset)}{\delta t} + \frac{\delta (1-\emptyset) u_i^f}{\delta x_i} = 0 \quad (2)$$

where $\emptyset$ and 1-$\emptyset$ are the particle and fluid volume fractions respectively, u_i^s and u_i^f are the sediment and fluid phase velocities respectively, x_i is the spatial dimension, t is time, and the index i = 1, 2, 3 represents the streamwise, spanwise, and vertical component, respectively. The momentum equations are written for each phase based on (Hsu et al., 2004), and the momentum equations for fluid and particle phases can be written as:

$$\frac{\delta \rho^s \emptyset u_i^s}{\delta t} + \frac{\delta \rho^s \emptyset u_i^s u_j^s}{\delta x_j} = -\emptyset \frac{\delta p}{\delta x_i} + \emptyset f_i - \frac{\delta p^s}{\delta x_i} + \frac{\delta \tau_{ij}^s}{\delta x_j} + \emptyset \rho^s g_i + M_i^{sf} + S_i^s \quad (3)$$

$$\frac{\delta\rho^f(1-\emptyset)u_i^f}{\delta t}+\frac{\delta\rho^f(1-\emptyset)u_i^f u_j^f}{\delta x_j}=-(1-\emptyset)\frac{\delta p}{\delta x_i}+(1-\emptyset)f_i+\frac{\delta\tau_{ij}^f}{\delta x_j}+(1-\emptyset)\rho^f g_i+M_i^{fs}+S_i^f \quad (4)$$

where ρ^s and ρ^f are the particle and the fluid densities respectively, g_i is the gravitational acceleration, f_i is an external volume force that drives the flow, p is the fluid pressure. τ_{ij}^f is the fluid stress (viscous stress and fluid Reynolds stresses), p^s is the normal stress of particles τ_{ij}^s is the particle shear stress, M_i^{fs} and M_i^{sf} are the interphase momentum transferring to jump conditions at solid-liquid interface and the different forces acting on the phase such as drag, lift, or added mass forces (Eqs. 5 and 6), and S_i^f and S_i^s are the Reynolds averaged momentum source terms representing the hydrodynamic forces imposed on the flow and the sediment, respectively, by the rotation of the turbine. A theory is required to determine these terms which will be explained in the next section.

$$M_i^{sf}=\emptyset(1-\emptyset)K\left(u_i^f-u_i^s\right)-\frac{1}{S_c}(1-\emptyset)Kv_t^f\frac{\delta\emptyset}{\delta x_i} \quad (5)$$

$$M_i^{fs}=-\emptyset(1-\emptyset)K\left(u_i^f-u_i^s\right)-\frac{1}{S_c}(1-\emptyset)Kv_t^f\frac{\delta\emptyset}{\delta x_i} \quad (6)$$

where K is the drag parameter, S_c is the Schmidt number, and ν_t^b is the turbulent viscosity. The two terms in Eqs. 5 and 6, containing the drag parameter, *K*, and the Schmidt number, S_c, on the right-hand side (RHS) represent the momentum coupling between the fluid phase and particle phase by drag force, the second term especially denotes the fluid turbulent suspension term, also called drift velocity by Simonin (1991). Therefrom, ν_t^b is the turbulent viscosity to be calculated using a turbulence closure model. The turbulence model k-ε described by Cheng et al. (2017) has been used. The drag parameter, *K*, is modeled following (Schiller & Naumann, 1933) following the relation:

$$K=0.75C_d\frac{\rho^f}{d_{eff}}\left\|u^f-u^s\right\|\beta^{-h_{Exp}} \quad (7)$$

where d_{eff} is the effective sediment diameter which multiplies the particle diameter by the shape factor ψ, C_d is the drag coefficient, $\beta^{-h_{Exp}}$ is the hindrance function that represents the drag increase when the particle volume fraction increases, such as $\beta = (1 - \emptyset)$, and $h_{Exp} = 2.65$ is the hindrance exponent that depends on the particulate Reynolds number (Re_p) in which $Re_p = (1 - \emptyset)\|u^f - u^s\|d_{eff}/v^f$, where v^f is the kinematic viscosity of the fluid. The drag coefficient C_d in Eq.7 depends on the particulate Reynolds number (Re_p), and is calculated as:

$$C_d = \begin{cases} \frac{24}{Re_p}\left(1 + 0.15Re_p^{0.687}\right), & Re_p \leq 1000 \\ 0.44, & Re_p > 1000 \end{cases} \quad (8)$$

The particle phase stress involves the particle normal stress or pressure p^s and the particle shear stress τ_{ij}^s. The particle pressure is classified into two components: a shear-induced or collisional component, p^{ss}, and a permanent contact component, p^{ff} (Johnson & Jackson, 1987):

$$p^s = p^{ff} + p^{ss} \quad (9)$$

p^{ff} represents the particle pressure due to the enduring contact between particles in a concentrated region when the particles are quasi static. This term is important to prevent an unphysical sediment concentration at the sediment bed when the sediment concentration is close to its maximum packing limit. It is calculated as:

$$p^{ff} = \begin{cases} 0, \emptyset < \emptyset_{min}^{Fric} \\ F\frac{\left(\emptyset - \emptyset_{min}^{Fric}\right)^{\eta_0}}{(\emptyset_{max} - \emptyset)^{\eta_1}}, \emptyset \geq \emptyset_{min}^{Fric} \end{cases} \quad (10)$$

Following (Chauchat et al., 2017), the limit values are fixed as $\emptyset_{min}^{Fric}$= 0.57 and $\emptyset_{max}$ = 0.635 for spheres and F, η_0, and η_1 are empirical coefficients.

Concerning the closure models for granular constraints, either for the shear induced or for the collisional stresses, the dense granular rheology is applied (Chauchat et al., 2014), so that the total particle phase shear stress can be calculated as follows, where represents a solid phase Reynolds stress and r_{ij}^{s} is the granular stress contribution defining the interactions between particles:

$$\tau_{ij}^{s} = R_{ij}^{s} + r_{ij}^{s} \qquad (11)$$

The granular contribution is written as:

$$r_{ij}^{s} = \mu_{Fr}^{s} + S_{ij}^{s} \qquad (12)$$

where the frictional viscosity μ_{Fr}^{s} is defined following Chauchat & Médale (2014), and S_{ij}^{s} is the deviatoric part of sediment phase strain rate tensor (Chauchat & Médale, 2014).

2.2. HydroKinetic turbine modeling

The hydrokinetic turbine is modeled using momentum theory. The model is a hybrid analytical Blade Element Momentum Theory (BEMT). This theory allows the hydro-dynamic behavior of the turbine to be modeled without requiring a blade resolved simulation.

2.2.1. BEMT

This model takes into consideration the effects of rotor geometry characteristics like chord and twist distributions of the blade airfoil. The blade is decomposed into radial sections since each of the blade elements has a different rotational speed and geometric characteristics, hence experiencing a slightly different flow.

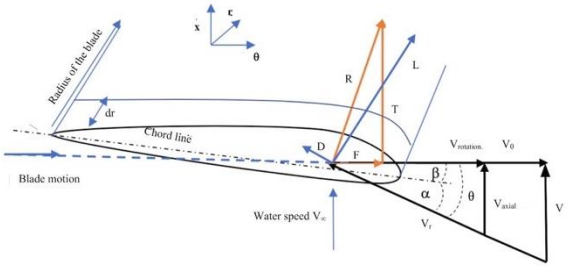

Fig. 1. Flow velocities and forces acting on the blade represented by BEMT. V_{axial} and V_θ are the axial and tangential velocity components respectively, β is the blade twist angle, α is the angle of attack and θ is the inflow angle.

The elementary forces and moments applied on each element are then integrated over the hole blade measurement. In the current study, the BEMT is used as the main computational method and it is applied over a disc that represents the turbine with radius, r, thickness, e, and number of blades n. The momentum source terms added to the momentum equations (Eqs. 3 and 4) are determined from the lift (L) and the drag (D) forces acting on each blade (Fig. 1). Those forces act, respectively, perpendicular and parallel to the relative velocity, V_r. They are estimated by relations (Eqs. 13 and 14), where c is the chord of the blade which varies as a function of the radius, C_L and C_D are lift and drag coefficients, respectively, their values depend on the geometry of the blade (angle of attack), F_{tip} is Prandtl's Loss Factor correction which is introduced to correct the loading for a finite number of blades (El khchine & Sriti, 2017).

$$L = 0.5\rho^f c V_r^2 C_L F_{tip} \qquad (13)$$

$$D = 0.5\rho^f c V_r^2 C_D \qquad (14)$$

the relative velocity of the water flow, V_r, depends on the axial and tangential fluid velocities, V_{axial} and V_θ respectively, and the turbine rotational velocity, ω, such as:

$$V_r = \sqrt{V_{axial}^2} + (r\omega - V_\theta)^2 \qquad (15)$$

The lift and drag forces are rotated into the rotor cylindrical coordinate system to obtain axial and tangential force components:

$$f_x = L\cos\theta + D\sin\theta \qquad (16)$$

$$f_\theta = -D\cos\theta + l\sin\theta \qquad (17)$$

The momentum sources are computed based on the time-averaged blade forces imparted by the blade onto the fluid. The source term, S_i, is projected in regards to the cylindrical coordinate system as S_x and S_θ such as follows:

$$S_x = -\frac{nf_x}{2\pi re} \qquad (18)$$

$$S_\theta = -\frac{nf_\theta}{2\pi re} \qquad (19)$$

where f_x and f_θ are the axial and tangential components respectively of the elementary forces defined in Eqs. 16 and 17, e is the thickness of the disc that represents the turbine.

The total thrust, T, and power, P, are calculated by numerical integration of the sources over the disc region in the cartesian coordinate system. The model is integrated numerically in OpenFOAM as a *C* + + code.

2.2.2. Validation

To ensure model accuracy, the experimental measurements of Mycek et al. (2014) have been used to validate the model. The experiments were performed in the Institut Français de Recherche pour l'Exploitation de la Mer (IFREMER) experimental flume tank, with a length L = 18 m, a width l = 4 m and a depth h = 2 m. The rotor of diameter d = 0.7 m is connected to a cylindrical hub of diameter d_h = 0.092 m (Mycek et al., 2014).

As previously mentioned, the turbine is represented numerically by a porous disc, and a solid disc is fixed on the center to represent the hub, on which the BEMT is applied and the momentum energy is extracted from the domain. The geometry and the mesh are created using ICEM CFD software, so the entire domain is divided into a mesh of 1.3 million structured hexahedral cells. The computational domain is a 4 m * 18 m * 2 m block. The disc of diameter d = 0.7 m is located at 11d downstream of the inlet, this leaves 14d

downstream of the disc to observe the development of the wake. The mesh of areas of interest is refined to concentrate computational accuracy. An averaged value of the incident flow velocity (0.8 m/s) is considered (Table 1). The blades are modeled using 23 discrete NACA 63418 elements along their span in accordance with the detailed blade profile description in Mycek et al. (2014).

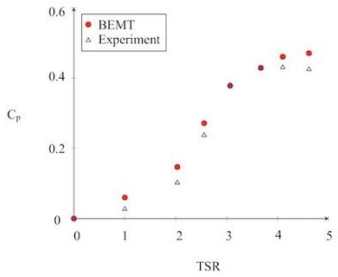

Fig. 2. Variation of power coefficient as a function of the TSR factor.

Table 1. Description of the parameters used in the Mycek et al. (2013) experiments; U_f : Incident flow velocity, TSR: Tip Speed Ratio (ω d/2U_f), and TI: Turbulence Intensity.

Profile	U_f (m/s)	TSR	Re	TI	Pitch angle	Rotation
NACA 63418	0.8	3.67	28 e4	3%	0°	Counterclockwise

Figure 2 shows a comparison of numerical results of the foregoing configuration with the experimental measurements of Mycek et al. (2014). As observed, the C_p evolution is in accordance with the experimental results as the TSR increases until 3.67. These results can be explained by the effect of the vortices generated on the tip of the blades since the vortices were considered from the beginning to be estimated using a simple correction on the tip, while in literature (Branlard & Gaunaa, 2014) other corrections for the BEMT might be considered.

2.3. Validation of the method

The measurements of the laboratory experiments done by Hill et al. (2014) under clear-water conditions, are used to validate the method that simulates the interaction of sediment and turbine. The simulated rectangular channel (Fig. 3) is 10 m long (streamwise direction, x), 2.75 m wide (crosswise direction, z) and 1.15 m deep (vertical direction, y). The rotor diameter of the turbine is d = 0.5 m. The center of the rotor is located 3 m from the inlet with a height of 0.425 m from the bed surface. The tip speed ratio is 7.1, and the bulk velocity of the fluid is 0.56 m/s. All the parameters are listed in Table 2. Concerning the boundary conditions, at the walls zero velocity is imposed. Within the OpenFOAM framework, for the total kinetic energy (TKE), a small fixed value can be used so that the kqRWallFunction acts similarly as a Neumann boundary condition. At the inlet, the velocity is set to a logarithmic profile with the distance to the wall y, where u_* = 0.027 m/s is the bed friction velocity. This value is chosen so that it is lower than the critical velocity (u_* = 0.034 m/s) to avoid sediment transport due to the flow. This profile is also set as an initial condition. At the outlet, the hydrostatic pressure is fixed. At the top, a slip condition is imposed. The real bottom is considered as impermeable. Other details and experimental setup are found in Hill et al. (2014). Concerning the sediment properties, sands of diameter 1.8 mm and density of 1922 kg/m^3 are placed in the bed with a volume fraction of 55%. The size of the time step for the flow simulation is 0.001 s. The turbine is modelled using the BEMT, the effect of the tower is not considered.

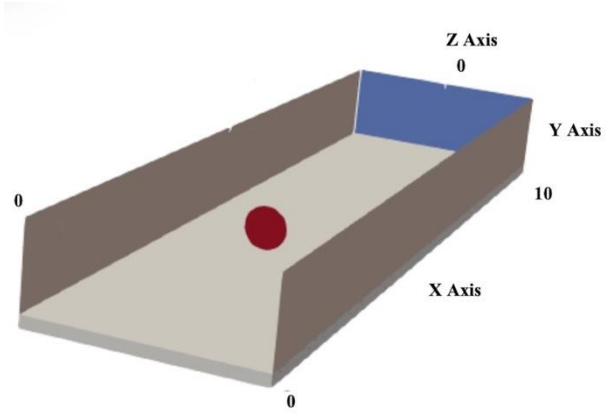

Fig. 3. Initial state of the domain, position of the disc at 3 *m* from the inlet and the sheet layer of sands on the bottom (grey color).

Table 2. Numerical properties for the simulation, where *s* is the initial thickness of the sand sheet and d_s is the mean sand diameter. Note that u_* is the bed friction velocity, a is the domain length in the x-direction, b is the water depth, and c is the length in the z-direction.

Hydro Properties				
a*b*c (m)	d (m)	TSR	U_f (m/s)	Turbulence model
$10 * 1.15 * 2.75$	0.5	7.1	0.56	$k - \varepsilon$
Sediment Properties				
φ (%)	s (m)	d_s (mm)	u_* (m/s)	Particle shear stress
55	0.15	1.8	0.027	Granular flow rheology

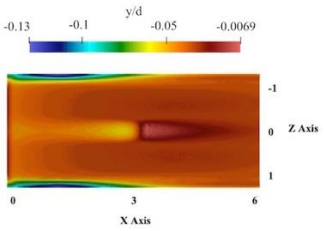

Fig. 4. Computed contours of bed elevation at t = 3 min, the turbine is located at x = 3 m.

Figure 4 shows the computed contours of bed elevation at 3 min, the turbine is located at x = 3 m. As can be seen, the scour occurred below the turbine and the deposition is clear in the downstream area. The computed temporal scour evolutions are compared with the measurements of Hill et al. (2014) and the numerical results of Yang et al. (2017) in Fig. 5 at two spanwise locations (z = 0 and z = 0.2d) 0.1d downstream of the turbine. As can be seen, the computed bed evolutions are nearly the same and show good agreement with the measurements and the LES results.

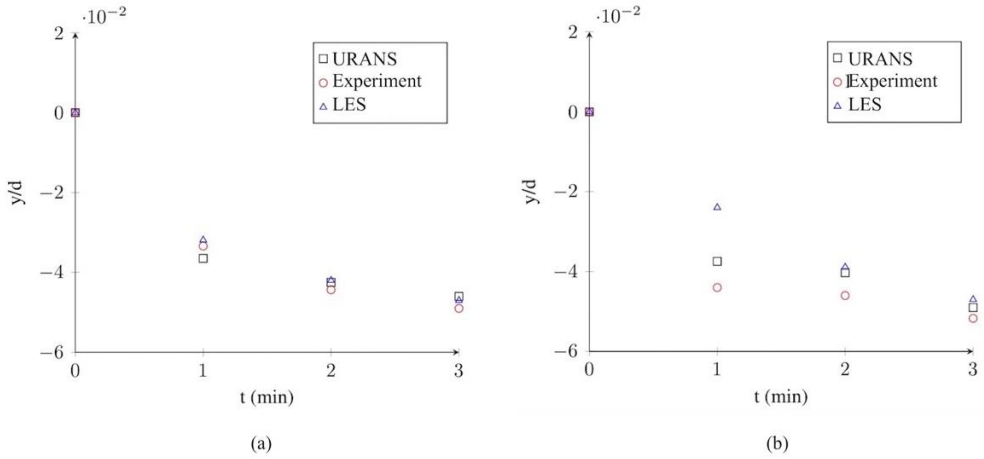

Fig. 5. Comparison of computed time series of bed elevation relative to the initial flat bed at 0.1d downstream from the rotor and at z = 0 (left), at z = 0.2d (right) (turbine is located at z = 0 in the span-wise direction): Measurements by Hill et al. (2014) (circle); multiphase Euler-Euler with BEMT, i.e. URANS (square); LES by Yang et al. (2017) (triangle).

3. Flume and turbine blockage effects on river bed erosion

An attempt has been made to simulate the impact of a hydrokinetic turbine on the sediment transport. This attempt consists of considering one sediment class, sand of one diameter, and a horizontal axis turbine with an axial flow direction corresponding to the riverine case. The approach is configured with two different dimensions of the computational domain: configurations *A* and *B*. The numerical properties are explained in the next section for both configurations.

3.1. Numerical configuration

Table 3 lists the numerical properties for both configurations. These properties are used either for baseline cases or for turbine cases. The sediment particles are made of medium sand, density ρ_s = 2650 kg/m^3 and diameter d_s = 0.25 mm. The fluid is water with density ρ_f = 1000 kg/m^3 and kinematic viscosity $v = 10^{-6}$ m^2/s. The computational domain for Configuration *A* is a 4 m $*$ 0.35 m $*$ 1 m block in x, y, and z directions, respectively. The disc of diameter d = 0.08 m that represents the energy extracted by the turbine, is placed 1.51 m downstream of the inlet (Fig. 6). The mesh is created using the OpenFOAM library package, block Mesh, and it is configured as a 60 million hexahedral mesh. A layer 0.05 m thick and composed of 61% sand is spread on the bottom. While Configuration B has been tested with a computational domain 4 m $*$ 0.35 m $*$ 0.4 m block in x, y, and z directions, respectively, which is covered by about 20 million hexahedral cells, the disc is placed at 1.51 m from the inlet. The velocity ratio (*TSR*) is 2.1 for both cases. Concerning the boundary conditions, at the walls, zero velocity is imposed. Within the OpenFOAM framework, for the TKE, a small fixed value can be used so the kqRWallFunction acts similarly as a Neumann boundary condition. At the inlet, the velocity is set to the logarithmic profile (Eq. 20) with the distance to the wall y, where $u_* = 3.69$ cm/s is the bed friction velocity (Chauchat et al., 2017), $\kappa = 0.41$ is the von Karman constant, and $k_s = 2.5d_s$ is the Nikuradse roughness length. This profile is also set as an initial condition. At the

outlet, the hydrostatic pressure is fixed. At the top, a slip condition is imposed. The real bottom is considered as impermeable.

$$\frac{u^f}{u_*} = \frac{1}{k} ln\left(\frac{30y}{k_s}\right) \qquad (20)$$

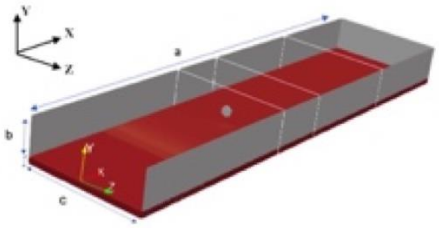

Fig. 6. Initial state of the computational domain, position of the disc and the sheet layer of the sand on the bottom (red color) and the three cross-sections (dashed-white lines) used for configurations *A* and *B*; *a*, *b*, and *c* are the length, depth, and width of the hydrodynamic channel, respectively (see Table 3).

Table 3. Numerical properties for both configurations A and B, where x_0 is the position of the turbine from the inlet, TI is the turbulence intensity, *s* is the initial thickness of the sand sheet, and d_s is the mean sand diameter. Note that the Froude number is $Fr = 0.466$.

Hydro Properties	A	B
dimensions a ∗ b ∗ c	4 ∗ 0.35 ∗ 1 (m)	4 ∗ 0.35 ∗ 0.4 (m)
d	0.08 (m)	0.08 (m)
x_0	1.51 (m)	1.51 (m)
TSR	2.1	2.1
TI	3%	3%
Turbulence model	k − ε	k − ε
mean-Velocity	0.8 (m/s)	0.8 (m/s)
blockage-ratio	0.0166	0.0416
Sediment Properties	A	B
φ	61%	61%
s	0.05 (m)	0.05 (m)

d_s	0.25 (mm)	0.25 (mm)
particle shear stress	granular flow rheology	granular flow rheology
model of friction	MuI (Hsu et al., 2003)	MuI (Hsu et al., 2003)
model of fluid viscosity model	Boyer (Hsu et al., 2003)	Boyer (Hsu et al., 2003)
of drag	Gidaspow (Hsu et al., 2003)	Gidaspow (Hsu et al., 2003)
model particle pressure	Lun (Lun, 1991)	Lun (Lun, 1991)

Table 3 lists the hydrodynamic and the transport properties of the configuration. Concerning the turbine, the blades are modeled using 23 discrete NACA 63418 elements among their span in accordance with the blade profile given in Mycek et al. (2014). The fluid turbulence model k-ε has been used for both configurations. A time step of 10^{-3} s is used to approach convergence.

Most of the critical stress, τ_c, calculations for setting sediment in motion are based on the work of Miedema (2010). The Shields parameter, denoted θ, establishes the relation between the friction force of the fluid and the force of the submerged weight of the sediment. The dimensionless friction or Shields parameter is defined by:

$$\theta_{cr} = \frac{\tau_c}{(\rho_s - \rho_f) g D_{50}} \qquad (21)$$

where τ_c is the critical friction stress exerted by the flow on the bottom. Referring to Miedema (2010), and considering the chosen sediment, the critical Shields parameter is θ_{cr} = 0.043. This corresponds to a critical shear stress value of 0.1738 Pa.

3.2. Results and discussions

Figures 7 and 8 show the modifications of the sediment bed due to the presence of the turbine for configurations A and B. Several changes in bed morphology have been found in the presence of the turbine. The clearest feature is the scour in the near wake area below the turbine, and the formation of a sediment deposition body downstream of the turbine. In addition, changes of the bed extend to the far wake zone in Configuration A compared to baseline morphology. The impact of the turbine on the transport of sediment is clear in both axial and transverse directions.

The bed morphology evolution near the turbine and downstream of its location, is widely different in both configurations. The effect of the wake generated behind the turbine

on the bottom is clearer for Configuration *A* (Fig. 7) than for Configuration *B* (Fig. 8). To more closely investigate the difference of the impact of the turbine between the two configurations, two transverse sections are taken into consideration. Such as S_1 at x_0 below the turbine, and S_2 at $x - x_0$ = 6d downstream of the turbine for both configurations. The temporal and spatial evolution of each section is examined in the next sections.

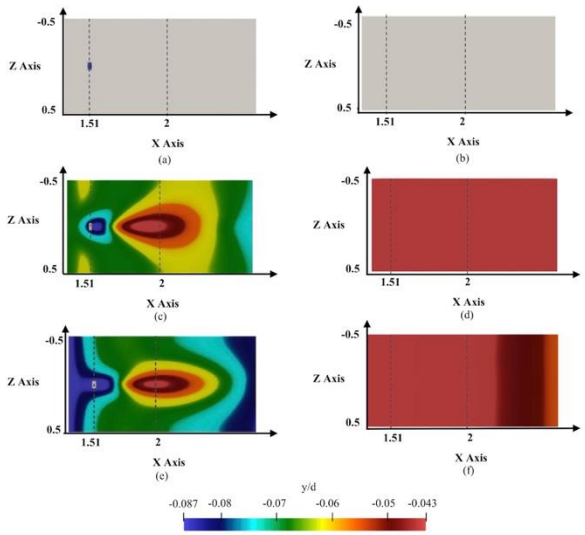

Fig. 7. Normalized elevations of the bottom (*y/d*) for the baseline case (right) and in the presence of the turbine (left) for Configuration *A*. (a,b) t = 0 s, (c,d) t = 40 s, and (e,f) t = 60 s.

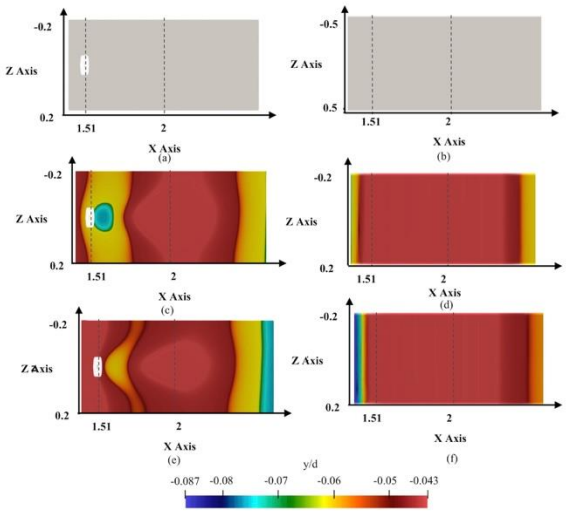

Fig. 8. Normalized elevations of the bottom (*y/d*) for the baseline case (right) and in the presence of the turbine (left) for Configuration *B*. (a,b) t = 0 s, (c,d) t = 40 s, and (e,f) t = 60 s.

3.2.1. Temporal evolution

Figure 9 shows the temporal evolution of the bed elevation for configurations A and B. In Configuration A, the scour below the turbine at S_1 (Fig. 9a), occurs in the first 30 s, the bed elevation decreases progressively to reach a scour of 0.09d. Without the turbine the bed elevation does not vary as much as in the case with the turbine, the maximum scour depth that occurred is 0.04d which is much lower than the scour depth when the turbine is installed. While the scour below the turbine for configuration B (Fig. 9c) is not as deep compared to Configuration A, it reaches a maximum depth of 0.07*d*. Concerning the temporal variations of the bed downstream of the turbine, Figs. 9b and 9d show that the erosion process is less substantial at section S_2 for both configurations during the 60 s of simulation regarding the scour below the turbine, whereas without the turbine the scour curve evolves differently. Moreover, at section S_2, a continuously slow erosion process is acting for Configuration A whereas a steady state seems to be reached with the turbine

occurring a maximum elevation of $-0.04d$ under the initial interface of the sand layer.

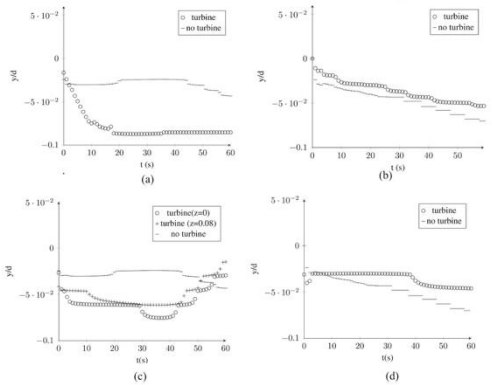

Fig. 9. Temporal evolution of normalized bed elevation (y/d) with and without the turbine at (a,c) S_1 and (b,d) S_2 respectively for Configurations *A* (upper) and *B* (lower).

Traditionally, the sediment transport and the erosion process are characterized by the bed shear stress and the critical bed shear stress. Particularly, Fig. 10a shows that the shear stress below the turbine in Configuration A is maximum in the first instants of the simulation then it continues to decrease until reaching 0.08 Pa. Note that this is lower than the critical erosion shear stress value of 0.1738 Pa. This could explain the stability of the scour below the turbine after t = 30 s, the during which bed shear stress below the turbine can no longer erode the sediment. At section S_2 ($x - x_0 = 6d$) (Fig. 10b), after t = 20 s, the shear stress decreases slowly around a value close to the critical shear stress for both situations (with and without the turbine). This is consistent with a slight bottom evolution. Note that, with the two-phase flow approach, erosion is not triggered by the bottom shear stress exceeding the critical stress. Here, agreement between the model and the erosion theory is found.

In Configuration B, in Figs. 10c and 9a, the bed elevation and the bottom shear stress do not vary as much as for Configuration A at S_1, and the erosion process evolves slowly compared to Configuration *A*. Even if the bottom elevation does not evolve a lot, the deposition and erosion processes can persist simultaneously. Moreover, the entrained matter can come from the lateral sides due to the turbine's rotation effect. Thus, the presence of the turbine increases the local shear stress directly below the turbine and reduces shear stress in the near wake zone (Fig. 10). The presence of the turbine also greatly enhances scour below the turbine (Figs. 9a and 9c).

The stability of the scour below the turbine for Configuration *A* can also be explained by the local flow acceleration resulting from flow shrinking between the rotor bottom tip and the top of the sand layer (e.g., Fig. 11 at t = 40 s). This acceleration decreases the sand layer below the turbine, forms scour, and subsequently leads to a varied morphology downstream of the turbine. Fig. 11 shows the swirl induced on the wake by the rotation of the turbine at t = 40 s in Configuration *A*. A simple temporal analysis on two locations is not enough to fully describe the process. A spatial analysis should be done, but at particular instants. The equilibrium state occurred below the turbine at t = 40 s in Configuration *A* (Fig. 9a) and the last instant is chosen to do this afterwards.

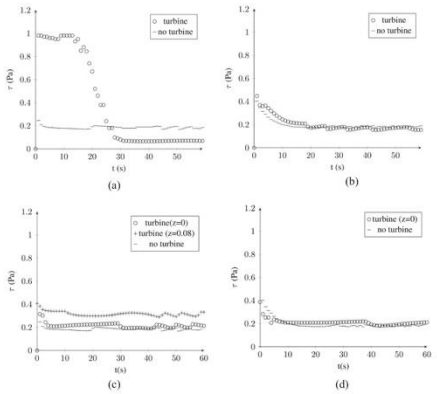

Fig. 10. Temporal evolution of bed shear stress with and without the turbine at section (a,c) S_1, (b,d) S_2, respectively, for configurations *A* (upper) and *B* (lower).

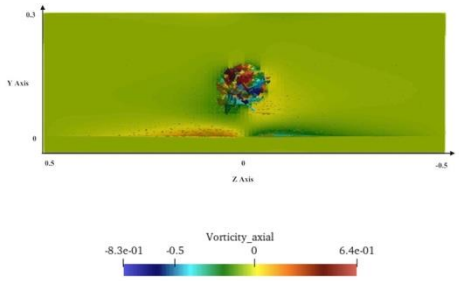

Fig. 11. Velocity field in the (y,z) plane colored by the fluid vorticity.

3.2.2. Spatial evolution

The baseline bed morphology evolution (Fig. 12) is similar between configurations *A* and *B* at both cross sections S_1 or S_2 at t = 40 s. Although, in the presence of the turbine, Fig. 12a shows that the maximum scour occurred below the turbine is 0.084*d* for Configuration *A* and 0.07*d* for Configuration *B* at t = 40 s, otherwise at t = 100 s (Fig. 12c), the scour *B* is not as deep as at t = 40 s, and the bed for Configuration *A* is more eroded under the edges of the turbine but remains at the scour under the center of the turbine as for t = 40 s.

Figures 12b and 12d, show that a phenomenon of sediment deposition occurs downstream of the turbine for Configuration *B* since the bed elevation is greater than the baseline bed elevation. These results illustrate that there is an important erosion process occurring in the wake of the turbine that leads to deposition of the sediment at 6*d* and to reach such a bed elevation. This erosion may be produced by the sudden variation of the lateral local shear stress (Fig. 13a), such that the eroded sediment hits the edges of the channel and they are transported by the wake to be deposited at 6*d*. Thus, the erosion is more important for Configuration *A* than for Configuration *B*. This difference in erosion should be taken into account in the analysis of the turbine's effects.

The turbine represented by an actuator *BEMT* model induces a thrust force and a tangential force, these produce a reduction of the axial velocity in the turbine's wake and an increase of the tangential velocity which produces a swirl close to the turbine. This effect is in Fig.11, and it is more visible in Fig. 15, where the vertical profiles of the z- component of the fluid velocity shows the impact of the turbine in the vertical axis across the turbine and in the wake zone. In the turbine's plane the tip speed could be observed whereas it vanishes at 6*d* behind the turbine. Figure 15 illustrates the high vorticity in the turbine's plane at the turbine's location, and then the reduction of the vorticity 6*d* downstream of the turbine. So, the swirl

produced by the turbine has a very local impact. These results also reveal the presence of a high vorticity close to the bottom in the turbine's plane (a) that should produce erosion beneath the turbine. This vorticity decreases with the distance to the canal axis. These results explain the localization of the erosion close to the turbine. Similar results have been obtained for Configuration A. Some differences appear in the vorticity intensities close to the bottom that could indicate the greater erosion encountered in the Configuration A beneath the turbine compared to Configuration B. These results could explain the scour occurring below the turbine for Configuration A at about 0.09*d* which is deeper than that of Configuration B of around 0.07*d* (Fig. 12a).

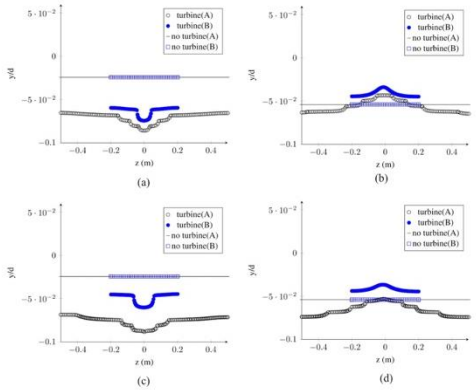

Fig. 12. Spatial evolution of bed elevation with and without the turbine at (a,b) sections S_1 and S_2 , respectively, at t = 40 s and (c,d) sections S_1 and S_2 , respectively, at t = 100 s for configurations A (black) and B (blue).

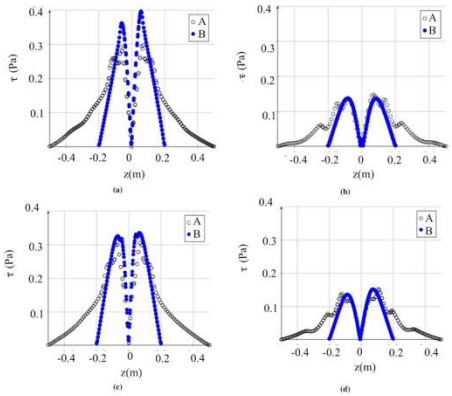

Fig. 13. Spatial evolution of shear stress (τ_{yz}) at (a,c) section S_1 and (b,d) section S_2 at t = 40 s (upper) and t = 100 s (lower) for configurations A (black) and B (blue).

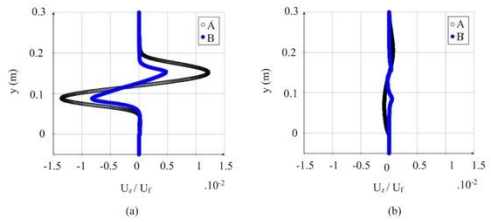

Fig. 14. Vertical profiles of velocity, normalized by the mean velocity of the fluid upstream of the turbine, U_f at sections S_1 (a) and S_2 (b) for configurations A and B at t = 40 s.

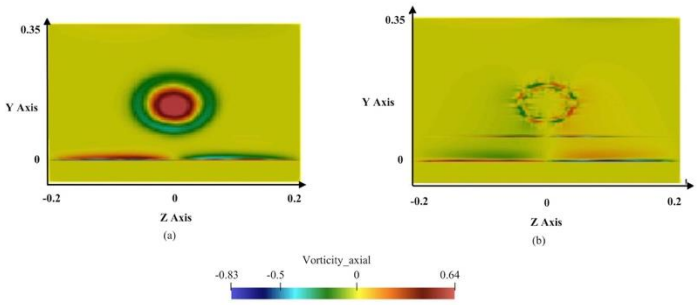

Fig. 15. Iso-contouring of the axial vorticity in cross section areas S_1 (a) and S_2 (b) for Configuration B at t = 40 s.

The drawing of the shear stress on the yz plane on the bottom (Fig. 13) confirms that the rotation of the turbine has a direct impact on the bed below the turbine (Fig. 13a). The maximum of the shear stress is encountered on both sides of the turbine and is clearly greater than the critical shear stress. The shear stress value is reduced for both cases downstream of the turbine (Fig. 13b) confirming a small implication of the swirl due to the rotation on the bed erosion far downstream of the turbine. Thus, Figs. 13 and 15 assure that the flow in the wake zone does not have the enough capacity to erode the bottom as occurs below the turbine, due to the reduction of the effect of the swirl on the bottom while moving away from the turbine. The differences encountered between the configurations *A* and *B* on the τ_{yz} (Fig. 13) shear stress appears as a result of the blockage effect.

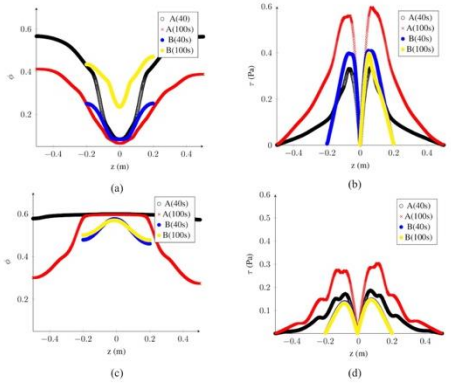

Fig. 16. Cross sectional profiles at y = 0 m of (a,c) sediment volume fraction ∅ and (b,d) shear stress τ_{yz} at sections (a,b) S_1 and (c,d) S_2, at t=40 s and 100 s.

Once the flow has stopped eroding the bed under the turbine for Configuration *A* at *t* = 40 s, then normally there should not be a lot of sediment which is transported in the wake behind the turbine. Figure 17a reveals that the volume fraction of sediment at y = 0 is not null but remains at φ = 0.1 under the turbine at t = 40 s and t = 100 s. This is just above the bed and is a witness for the low concentration layer. This sediment can be carried away by the flow easily. It could come from both sides of the turbine as the shear stress due to the rotation is still high (around 0.33 Pa) (Fig. 16b) and the erosion process could still take place. Downstream of the turbine, the sediment layer is more condensed (Fig. 16c) and the shear stress in the yz plane at this layer (Fig. 16d) remains close to the critical value.

It is important to see what is going on downstream of the turbine for Configuration *A*, and compare the results with those of Configuration *B*, considering that there is a significant difference between the results of the two configurations as shown in Fig. 16. Figure 17 compares the evolution of the bed morphology in the axial direction between configurations *A* and *B*. The scour generated below the turbine is very clear for Configuration *A* with a maximum value of depth of 0.09*d*, contrary to the scour occurring below the turbine for Configuration *B* which reaches a maximum value of depth of 0.07*d*.

These values are also shown below the turbine in Fig. 12. The turbine greatly enhances a depositional dune downstream of its location in configurations *A* and *B*.

Figure 18 shows the difference in the dimensionless bed elevation between the baseline and turbine results at S_1 and S_2 for both configurations. The impact of the turbine for Configuration A on the erosion process under its location is the most significant at time t = 40 s (Fig. 18a) and at the transverse section at t = 40 s (Fig. 18b). Otherwise, the sediment deposition process is more obvious for Configuration B at section S_2 at time t = 40 s (Fig. 18a) and in the transverse section at t = 40 s (Fig. 18b). Although the impact of the turbine at S_2 does not differ between both configurations as much as at S_1.

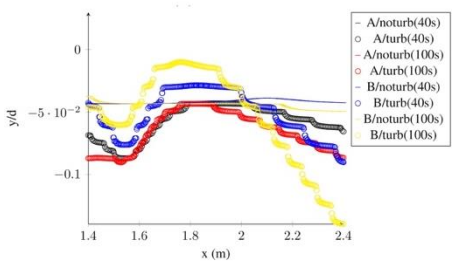

Fig. 17. Spatial evolution of bed morphology *y/d* on the bottom of the channel for configurations A and B at t = 40 s and t = 100 s, with (turb) and without (noturb) the turbine.

Furthermore, the blockage effect can be distinguished, when comparing the impact of the turbine between the configurations. The erosion process under the turbine is more obvious surprisingly for the lower blockage ratio case (Configuration A) (Fig. 17). Concerning the transport of sediment, the impact of the turbine in Configuration A is very localized under its location (Fig. 17), but in Configuration B the erosion is more distributed throughout the entire width of the channel at the level of the turbine (Fig. 17). This can be explained by an

interaction in Configuration B between the presence of the walls of the channel and the presence of the turbine. The effect of closed walls leads to bidimensional flow (little variation in z). From an hydrodynamic point of view, Fig. 19a shows that the vorticity is important in Configuration A under the turbine but it is decreasing while moving away from its location, so that it is almost null at the lateral sides of the channel. On the other hand, the vorticity in Configuration B is still substantial throughout almost the entire width of the channel at the turbine level (Fig. 19b). To explain this result, it is hypothesized that the high confinement induces a strong interaction between the channel side effects and the turbine's effect. This leads to a distribution of the vorticity over the entire width, and, thus, reduces vorticity intensity and its capability to erode the bed. Consequently, the erosion under the turbine for Configuration B is lower than for Configuration A and is not yet established at t = 40 s. Moreover, the transport of sediment is more stable for Configuration *A* than for Configuration *B*. In addition, the 3D effect of the turbine over cross sectional areas (Fig. 15) is clearer for Configuration *A* than for Configuration *B*, such as the vorticity fields are widespread below the turbine on both sides resulting in increasing bottom shear stress (Fig. 13a) and more erosion of the bottom near the edges of the channel (Fig. 12a).

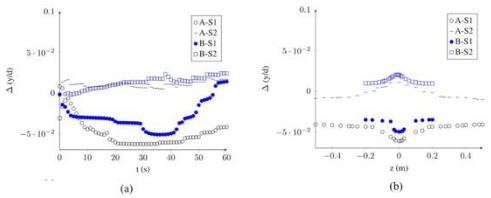

Fig. 18. Difference in dimensionless bed elevation between the baseline and turbine results at S_1 and S_2, the erosion is represented as negative values. (a): temporal evolution of ($\Delta y/d$), and (b): spatial evolution of $\Delta y/d$ laterally in the cross section at time t = 40 s.

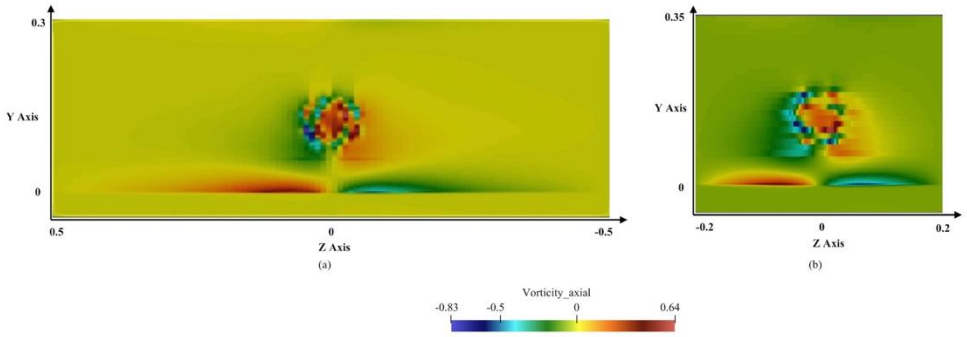

Fig. 19. Iso-contouring of the axial vorticity at cross section area S_1 for configurations A (a) and B (b) at t = 40 s.

4. Conclusions

The research reported here coupled a 3D Euler multiphase model CFD approach with a BEMT model of an axial-flow, three-bladed hydrokinetic turbine to study the interactions between the turbine and sediment transport of sandy bed. A validation of the different parts of the model has been done. A first study of the erosion of a bottom substrate has been done to estimate the impact of the studied turbine on a sandy river bottom and to highlight the blockage effect on the mobile sediment bed. The energy extracted by the turbine alters the hydrodynamics of the stream by increasing or reducing the friction in areas around the turbines. Close to the turbine, scour phenomena and deposition zones appear.

The results show a significant impact of the blockage ratio on the evolution of the morphology of the bottom downstream of the turbine; the lower the ratio is, the more the impact of the turbine in the near wake zone is obvious. These results are consistent with experimental results of Williams et al. (2019) who investigated the scouring mechanism around a cylinder. They studied the effect of the ratio of cylinder diameter and the channel width on the erosion produced at the cylinder's location. They showed that there is an important effect of the proximity of the lateral walls on the erosion of the sediment bottom and that the stronger the blockage, the more the side walls have an impact on erosion. However, this comparison must be mitigated, because according to their experiences the importance of the lateral walls is only true if the ratio D/d_s (pier diameter to sediment diameter) exceeds 100. The current results are not obtained for a vertical cylinder but for a 80 mm diameter turbine with the sediment diameter being 0.25 mm. Configuration A considers a blocking rate of 0.0166 and Configuration B considers a blocking rate of 0.0416. These values are close to those used in the experiment of Williams et al. (2019). In addition, the ratio of the turbine diameter to the sediment diameter is 320.

Those computed morphology changes should have an impact on ecological processes. In the near field, the high levels of transported sediment could affect the surrounding water quality such as increasing the turbidity level, thus reducing the light penetration in water, the temperature, and the aquatic habitat. Moreover, metallic contaminants, in the case of different types of sediment, could be trapped in the sediment bed (Coynel et al., 2016) and be reintroduced to the water column by the erosion of the bed.

Large scale morphological evolution has also been considered such as the migration of dunes. Such evolution could modify the turbulent boundary layer and cause time-varying turbulent structures, which could then affect human daily activities such as farming (Awang et al., 2017) and can lead to economic losses and damages in the long term due to bank failure.

River morphology changes need thorough investigation as any excessive

development may also contribute to several impacts on river morphology. A need for a systematic investigation on turbine-sediment interactions remains for different blockage ratios and different sediment diameters. It will also be important to investigate in the future the impact of the displacement of an array of turbines on the transport of sediment.

5. Acknowledgments

The authors acknowledge CRIANN (Centre Régional Informatique et d'Application Numériques de Normandie) co financed by the Normandy Region, the French State, and the European Union, for access to the computational means and to the Manche Country Council for their funding. This work is financed firstly by the Lebanese District of Nakhleh, then by CG 50 of French District of Manche and the University of Caen.

References

Ahmed, U., Apsley, D. D., Afgan, I.,. Stallard, T., & Stansby, P. K. (2017). Fluctuating loads on a tidal turbine due to velocity shear and turbulence: Comparison of CFD with field data. *Renewable Energy*, *112*, 235–246.

Amoudry, L. O. (2014). Extension of $k-\omega$ turbulence closure to two-phase sediment transport modelling: Application to oscillatory sheet flows. *Advances in Water Resources*, *72*, 110– 121.

Apsley, D., Stallard, T., & Stansby, K. (2018). Actuator-line CFD modelling of tidal-stream turbines in arrays. *Journal of Ocean Engineering and Marine Energy*, *4*, 259–271.

Awang, A., Awang, N., Ariffin, J., Razi, M., & Abdullah, J. (2017). Environmental degradation: A review on the potential impact of river morphology. *MATEC Web of Conferences*, 103, 04001.

Bakhtyar, R., Yeganeh-Bakhtiary, A., Barry, D. A., & Ghaheri, A. (2009). Two-phase hydro- dynamic and sediment transport modeling of wave-generated sheet flow. *Advances in Water Resources*, *32*(8), 1267–1283.

Barbry, N., Guillou, S., & Nguyen, K. D. N. (2000). Une approche diphasique pour le calcul du transport sédimentaire en milieux estuariens. *Comptes Rendus de l'Académie des Sciences, série II B*, 328–793. (in French)

Branlard, E., & Gaunaa, M. (2014). Development of new tip-loss corrections based on vortex theory and vortex methods. *Journal of Physics Conference Series*, 555, 012012.

Chauchat, J., & Guillou, S. (2008). On turbulence closures for two-phase sediment-laden flows models. *Journal of Geophysical Research, 113*, C11017.

Chauchat, J., & Médale, M. (2014). A three-dimensional numerical model for dense granular flows based on the rheology. *Journal of Computational Physics*, *10*(1016), 696–712.

Chauchat, J., Cheng, Z., Nagel, T., Bonamy, C., & Hsu, T. J. (2017). Sedfoam-2.0: A 3-d two-phase flow numerical model for sediment transport, *Geoscientific Model Development*, *10*, 4367–4392.

Chen, L., & Lam, W. H. (2014). Slipstream between marine current turbine and seabed. *Energy*, *68*, 801–810.

Chen, L., Hashim, R., Othman, F., & Motamedi, S. (2017). Experimental study on scour profile of pile-supported horizontal axis tidal current turbine. *Renewable Energy*, *114*, 744–754.

Cheng, Z., Hsu T.-J., & Calantoni, J. (2017). Sedfoam: A multi-dimensional Eulerian two-phase model for sediment transport and its application to momentary bed failure. *Coastal Engineering*, *119*, 32-50.

Consul, C. A., Willden, R. H. J., & McIntosh, S. C. (2012). Blockage effects on the hydrodynamic performance of a marine cross-flow turbine. *Philosophical Transactions of the Royal Society A*, *371*, 20120299.

Coynel, A., Gorse, L., Curti, C., Schafer, J., Grosbois, C., Morelli, G., Mojtahid, M. (2016). Spatial distribution of trace elements in the surface sediments of a major European estuary (Loire Estuary, France): Source identification and evaluation of anthropogenic contribution. *Journal of Sea Research*, *118*, 77–91.

El-khchine, Y., & Sriti, M. (2017). Tip loss factor effects on aerodynamic performances of horizontal axis wind turbines. *Energy Procedia*, *118*, 136-140, 1876-6102.

Fairley, I., Masters, I., & Karunarathna. H. (2015). The cumulative impact of tidal stream turbine arrays on sediment transport in the Pentland Firth. *Renewable Energy*, *80*, 755–

769.

Garrett, C., & Cummins, P. (2007). The efficiency of a turbine in a tidal channel. *Journal of Fluid Mechanics*, *588*, 243–251.

Gillibrand, P., Walters, R., & Mcilvenny, J. (2016). Numerical simulations of the effects of a tidal turbine array on near-bed velocity and local bed shear stress. *Energies*, *9*, 852.

Grondeau, M., Mercier, P., Guillou, S., Poirier, J., Poizot, E., & Méar, Y. (2017). Numerical simulation of a tidal turbine model in a turbulent flow with the lattice Boltzmann method. Proceedings, *12th European Wave and Tidal Energy Conference*, (pp. 28–31), August 27-September 1, 2017, Cork, Ireland.

Guillou, S., Thiébot, J., Chauchat, J., Verjus, R., Besq, A., Nguyen, D. H., & Pouv, K. (2011). The filling dynamics of an estuary: From the process to the modelling. In: *Sediment transport in aquatic environments*. (pp. 125-146), intech.

Hill, C., Musa, M., Chamorro, L. P., Ellis, C., & Guala, M. (2014). Local scour around a model hydrokinetic turbine in an erodible channel, Journal *Hydraulic Engineering*, *140*(8), 04014037.

Hill, C., Musa, M., & Guala, M. (2015). Interaction between instream axial flow hydrokinetic turbines and unidirectional flow bedforms. *Renewable Energy*, *86*, 409–421.

Hsu, T.- J., Jenkins, J. T. & Liu, P. L.- F. (2003). On two- phase sediment transport: Dilute flow. *Journal of Geophysical Resources*, *108*, 3057.

Hsu, T-J, Jenkins, J. & Liu, P. (2004). On two-phase sediment transport: Sheet flow of massive particles. *Proceedings of The Royal Society A: Mathematical, Physical and Engineering Sciences*, *460*, 2223-2250.

Jenkins, J. T., & Hanes, D. M. (1998). Collisional sheet flows of sediment driven by a turbulent fluid. *Journal of Fluid Mechanics*, *370*, 29–52.

Johnson, P. C., & Jackson, R. (1987). Frictional-collisional constitutive relations for granular materials, with application to plane shearing. *Journal of Fluid Mechanics*, *176*, 67–93.

Lun, C. (1991). Kinetic theory for granular flow of dense, slightly inelastic, slightly rough spheres. *Journal of Fluid Mechanics*, *233*, 539–559.

Malki, R., Williams, A. J., Croft, T. N., Togneri, M., & Masters, I. (2012). A coupled blade element momentum–computational fluid dynamics model for evaluating tidal stream turbine performance. *Applied Mathematical Modelling*, *37*, 3006–3020.

Miedema, S. A. (2010). Constructing the Shields curve, a new theoretical approach and its applications. Proceedings, *World Dredging Conference XIX*, September 9-14, 2010, Beijing, China.

Musa, M., Heisel, M., & Guala, M. (2018). Predictive model for local scour downstream of hydrokinetic turbines in erodible channels. *Physical Review Fluids*, *3*(2).

Musa, M., Hill, C., & Guala, M. (2019). Interaction between hydrokinetic turbine wakes and sediment dynamics: Array performance and geomorphic effects under different siting strategies and sediment transport conditions. *Renewable Energy*, *138*, 738–753.

Mycek, P., Gaurier, B., Germain, G., Pinon, G., & Rivoalen, E. (2014). Experimental study of the turbulence intensity effects on marine current turbines behaviour, Part I: One single turbine. *Renewable Energy*, *66*, 729-746.

Neill, S., Litt, E., Couch, S., & Davies, A. (2009). The impact of tidal stream turbines on large-scale sediment dynamics. *Renewable Energy*, *34*(12), 2803–2812.

Nguyen, K. D., Chauchat, J., Guillou, S., & Barbry, N. (2009). A two-phase numerical model for suspended-sediment transport in estuaries. *Advances in Water Resources, 32*, 1187–1196.

Nguyen, V. T., Guillou, S., Thiebot, J., & Santa Cruz, A. (2016). Modelling turbulence with an actuator disk representing a tidal turbine. *Renewable Energy*, *97*, 625–635.

Nishino, T., & Willden, R. H. J. (2012). Effect of 3-d channel blockage and turbulent wake mixing on the limit of power extraction by tidal turbines. *International Journal of Heat and Fluid Flow*, *37*, 123– 135.

Paola, C. & Voller, V. R. (2005). A generalized Exner equation for sediment mass balance. *Journal Geophysical Research*, *110*, F000274.

Ramirez-Mendoza, R. (2018). Laboratory study on the effects of hydrokinetic turbines on hydrodynamics and sediment dynamics. *Renewable Energy*, *129*, 271-284.

Schluntz, J., & Willden, R. H. J. (2015). The effect of blockage on tidal turbine rotor design and performance, Renewable Energy, *81*, 432–441.

Shields, M. A., Woolf, D. K., Grist, E. P. M., Kerr, S. A., Jackson, A. C., Harris, R. E., ... & Side, J. (2011). Marine renewable energy: The ecological implications of altering the hydrodynamics of the marine environment. *Ocean & Coastal Management*, *54*, 2–9.

Shives, M., & Crawford, C. (2016). Adapted two-equation turbulence closures for actuator disk RANS simulations of wind and tidal turbine wakes. *Renewable Energy*, *92*, 273–292.

Schiller, L. & Naumann, A.Z. (1933). *Zeitschrift des Vereines Deutscher Ingenieure*, *77*, 318-320.

Simonin., O. (1991). Prediction of the dispersed phase turbulence in particle-laden jets. *Gas–Solid Flows ASME–FED*, *121*, 197–206.

Thiébot, J., Bailly-du-Bois, P., & Guillou, S. (2015). Numerical modeling of the effect of tidal stream turbines on the hydrodynamics and the sediment transport – application to the alderney race (raz blanchard), France. *Renewable Energy*, *75*, 356–365.

Uh-Zapata, M., Pham-Van-Bang, D., & Nguyen, K. D. (2018). Parallel simulations for a 2d x/z two-phase flow fluid-solid particle model. *Computers and Fluids*, *2*, 103–110.

Williams, P., Balachandar, R., & Bolisetti, T. (2019). Examination of blockage effects on the progression of local scour around a circular cylinder. *Water*, *11*, 2631.

Xia, J. Q., Falconer, R. A., & Lin, B. (2010). Impact of different tidal renewable energy projects on the hydrodynamic processes in the Severn Estuary. UK, *Ocean Modelling*, *32*, 86–104.

Yang, X., Khosronejad, A., & Sotiropoulos, F. (2017). Large-eddy simulation of a hydrokinetic turbine mounted on an erodible bed. *Renewable Energy*, *113*, 1419-1433.